RSC Advances

Enhancing the corrosion resistance and surface biocativity of calcium-phosphate coating on biodegradable AZ60 magnesium alloy via a simple fluorine post-treatment method

Journal:	*RSC Advances*
Manuscript ID:	RA-ART-06-2015-010315
Article Type:	Paper
Date Submitted by the Author:	01-Jun-2015
Complete List of Authors:	Su, Yingchao; Jilin University, College of Materials Science and Engineering Lu, Yanbo; Jilin University, College of Materials Science and Engineering Su, Yichang; Jilin University, College of Materials Science and Engineering Hu, Jiangjiang; Jilin University, College of Materials Science and Engineering Lian, Jianshe; Jilin University, Li, Guangyu; Jilin University,

Enhancing the corrosion resistance and surface biocativity of calcium-phosphate coating on biodegradable AZ60 magnesium alloy via a simple fluorine post-treatment method

Yingchao Su, Yanbo Lu, Yichang Su, Jiangjiang Hu, Jianshe Lian, and Guangyu Li†

Key Laboratory of Automobile Materials, Ministry of Education, College of Materials Science and Engineering, Jilin University, Changchun 130025, China

Abstract

Biocompatible coatings, such as calcium phosphate (CaP), have been applied on biodegradable magnesium and its alloy to control their rapid degradation rates. This paper reports a further enhancement to CaP coating performance by applying a simple fluorine post-treatment on a CaP coating to form an F-CaP composite coating. The CaP coating was first deposited on AZ60 magnesium alloy samples via a phosphating method, then subjected to different post-treatment solutions to obtain F-CaP composite coatings. The effects of pH and time of the post-treatment were analyzed and the optimal corrosion resistance was obtained at pH 12 for 2 h. The F-CaP coating was consisted of mainly fluoridated hydroxyapatite, tricalcium phosphate and magnesium fluoride. Electrochemical corrosion measurement in simulated body fluid revealed that polarization resistance of the F-CaP coating is about 3 and 26 times higher than those of the HA and CaP coating, respectively, due to its denser coating structure and smoother surface. During immersion tests, the F-CaP coating also exhibited an improved corrosion resistance with

† Corresponding author. E-mail: guangyu@jlu.edu.cn

Tel: 86-431-85095875 Fax: 86-431-85095876

more active biomineralization than the CaP and HA coatings. This fluorine post-treatment offers a novel practical approach in improving the biodegradation behavior of CaP coatings on biodegradable magnesium implants.

Keywords

Magnesium alloy; Calcium phosphate coating; Fluoridated hydroxyapatite coating; Post-treatment; Biodegradable property.

1. Introduction

Magnesium (Mg) and its alloys have attracted considerable attention as potential alternative materials to biodegradable polymers for temporary medical implant materials.[1-3] Magnesium is degradable in human body, thus implants made of Mg alloys will not require a secondary removal surgery.[4] In addition to their biodegradability, Mg alloys are much closer to natural bone in density (Mg alloys: 1.74-2.0 g/cm^3; bone: 1.8-2.1 g/cm^3) and elastic modulus (Mg alloys: 41-45 GPa; bone: 3-20 GPa).[1, 2] However, their low corrosion resistance is considered as the main limitation for their clinical translation. Rapid degradation of an Mg implant may cause an abrupt loss of its mechanical integrity before the tissues sufficiently heal, and the created hydrogen gas pockets can potentially loosen the connection between the implant and the tissues.[5]

Surface modification of Mg alloys with a biocompatible coating can control the degradation rate during the required healing period while also improve implant/tissue interaction. Calcium phosphate (CaP) coatings, such as dicalcium phosphate dihydrate (DCPD), hydroxyapatite (HA) and tricalcium phosphate (TCP), offer intrinsic bioactivity and biocompatibility due to Ca and P which are the main elements in bone minerals.[6-9] Among these, HA is the most preferred coating material, because it has chemical and structural resemblance to natural bone and can accelerate bone concrescence.[10] However, the relatively high dissolution rate of HA coating compromises the *in vivo* stability and increases the potential for implants to loosen from their attachment to the bones.[6, 11]

Incorporation of fluorine into HA could effectively reduce the dissolution rate while maintaining the comparable biocompatibility.[11, 12] Although many methods have been developed for the

processing of fluoridated HA (FHA, $Ca_{10}(PO_4)_6(OH)_{2-x}F_x$, where $0<x<2$) coatings on Ti alloys,[12-15] to our best knowledge, electrodeposition has been the only method for depositing FHA coatings on Mg alloys, through adding 2 mmol/L fluoride directly into the electrolyte for HA preparation.[16-19] However, this practice exhibits low efficiency due to the small quantity of fluoride in the electrolyte and it is also difficult to apply universally to other coating methods.

As an inexpensive and easily prepared CaP to deposit onto metallic substrates, DCPD has been used as a precursor and transformed into HA coating through an alkali post-treatment.[20-24] Compared with the direct synthesis methods, it is easier to modify the crystal size through homogeneous precipitation of DCPD, which can then be converted to HA.[25] In our previous work,[26, 27] a CaP conversion coating was first deposited on the magnesium alloy, and then transformed into an HA coating through an alkali post-treatment. However, the preparation of FHA coatings through post-treatment has not been investigated as yet. Thus the aim of this paper is to introduce a modified post-treatment on a CaP coating in order to broaden the method for the preparation of FHA coatings and explore the effect of the post-treatment on the biodegradation behavior of the CaP coating in simulated body fluid (SBF).

2. Materials and methods

2.1. Sample preparation

An AZ60 magnesium alloy was used as the substrate and its composition is given in Table 1. Samples with dimensions of 10 mm × 10 mm × 5 mm were treated in a phosphating bath containing 11 g/L $Ca(NO_3)_2•4H_2O$, 1.2 g/L CaO, 8 mL/L H_3PO_4(85% V/V) and 0.5 g/L $Na_2MoO_4•2H_2O$, for 20 min to obtain a CaP conversion coating. The details of the coating

process were described in our previous work.[26] The CaP coating was then fluorine post-treated in NaF-NaOH mixed solutions at 80 °C to obtain the final coating. The fluorine post-treatment solution containing 5 g/L NaF was adjusted to various pH values by adding NaOH. In order to obtain optimum fluorine post-treatment conditions, two variable parameters were chosen: solution pH values (10, 11, 12, and 13) and treatment time (0.5, 1, 2 and 6 h). For comparison purposes, the CaP coating was also alkali post-treated in 1 mol/L NaOH solution at 80 °C for 2 h to obtain an HA coating.[26, 27]

2.2. Surface characterizations

The phases of the samples with and without coatings were characterized by X-ray diffraction (XRD, Rigaku Dymax, Japan) with Cu Kα radiation (λ=0.154178 nm) and a monochromator at 40 kV and 200 mA with the scanning rate and step of 4°/min and 0.02°, respectively. Surface chemical composition of the samples was analysed by X-ray photoelectron spectroscopy (XPS, ESCALAB Mk II, VG Scienta, Sweden) spectrometer using non-monochromatic Al Kα radiation of 240 W. Surface morphology and elemental composition of the coatings were identified by scanning electron microscopy (SEM, ZEISS EV018, Germany) equipped with an energy dispersive X-ray spectrometer (EDS, X-Max, Oxford Instruments, UK).

2.3. In vitro degradation studies

Degradation behavior of the coated samples were evaluated by using electrochemical and immersion tests in SBF at 37 °C. The SBF solution was composed of 8.0 g/L NaCl, 0.4 g/L KCl, 0.14 g/L $CaCl_2$, 0.35 g/L $NaHCO_3$, 1.0 g/L $C_6H_6O_6$ (glucose), 0.2 g/L $MgSO_4 \cdot H_2O$, 0.1 g/L $KH_2PO_4 \cdot H_2O$ and 0.06 g/L $Na_2HPO_4 \cdot H_2O$, and its pH=7.4.[28] The electrochemical measurements

were performed using a potentiostat (VersaSTAT3, Princeton Applied Research, US) with a three-electrode system where platinum, saturated calomel electrode (SCE, +0.242 V vs. SHE), and the samples (with 0.5 cm^2 exposed area) served as the counter, reference and working electrodes, respectively. Prior to the measurements, the samples were immersed in the SBF solution for about 30 min to establish the open circuit potential (OCP) or the steady state potential. Electrochemical impedance spectroscopy (EIS) measurements were carried out in a frequency range from 100 kHz down to 10 mHz at OCP values, with a root-mean square potential amplitude of 10 mV. The impedance data was displayed as Nyquist plots. The potentiodynamic polarization test was carried out at a scanning rate of 5 mV/s with a potential range of ±1.5 V from the OCP. The data for potentiodynamic polarization and EIS curves were analyzed using CorrView and ZSimpWin softwares, respectively.

The immersion tests were carried out in SBF for 7 and 15 days, and each sample was immersed in the SBF separately (ratio of SBF volume (mL) to sample surface area (cm^2) = 50). The temperature of the solution was controlled at 37 °C with a water bath. The hydrogen volume and pH of the SBF were recorded during the immersion. The surface morphologies of the samples after immersion for 7 and 15 days were observed with SEM and EDS. Then the corrosion products were removed using a chromic acid solution (200 g/L CrO_3 solution saturated with $AgNO_3$), and the surfaces after corrosion product removal were scanned using a photo scanner (Epson Perfection 2400, US).

3. Results and discussion

3.1. Determination of the optimum fluorine post-treatment parameters

In order to determine the optimum fluorine post-treatment parameters (pH of the solution and

treatment time), corrosion behavior of the coated samples was assessed by potentiodynamic polarization. Polarization curves of the coatings obtained at different pH values and treatment times are shown in Fig. 1, and the values of the electrochemical parameters obtained from the curves are summarized in Table 2. When the pH increased from 10 to 12 (Table 2), the corrosion potential (E_{corr}) shifted around 560 mV in the positive direction, the corrosion current density (i_{corr}) decreased by about 7 times, the polarization resistance (R_p) increased approximately 30 times, and the anodic branch showed a more passivation behavior. But when the pH increased beyond 12, the protective performance gradually deteriorated, although obvious passivation also occurred in the anodic branch. Similar trend is also observed in function of the treatment time, but with a lesser degree of change in the i_{corr}.

Typical SEM micrographs and corresponding EDS results of fluorine post-treated coatings at different pH and treatment times are showed in Fig. 2. Obviously, the microstructure of the coatings is strongly influenced by these two parameters. At a lower pH (Fig. 2a), the outer flake-like coating seemed unable to cover the whole surface; while the inner coating displayed a "dry-riverbed" microstructure with many cracks, which is probably composed of MgF_2 and $Mg(OH)_2$ phases judging from the high contents of F, O and Mg and the low levels of Ca and P (Fig. S1a). When the pH reached 12, the substrate was completely covered by the flake-like coating, and the content of F decreased to the comparable levels of Ca and P (Fig. 2b). However, when the pH increased to 13, clusters of white floccule were deposited on the coating, and the coating was unable to completely cover the substrate again (Fig. 2c). It seemed that the fluorine post-treatment at pH 12 could provide the dense and uniform coating structure. However, when the treatment time was extended to 6 h at pH 12 (Fig. 2d), the coating flakes seemed to be partly

dissolved, which can also be deduced from the dramatic decrease of the P content in the EDS result. A large number of ball-like precipitates emerged on the exposed substrate and in the gaps among the remaining coating flakes, and these ball-like precipitates are probably composed of MgF_2, CaF_2 and NaF phases, because the F content was shown to be extremely high (around 60 at.%) from the EDS spectrum (Fig. S1b). According to the microstructure evolution in function of the pH and the treatment time and the corresponding polarization results, the fluorine post-treatment at pH 12 for 2 h provides the optimum corrosion resistance for the Mg alloy. Therefore, it was employed in the following treatment and the resulting coating was labeled as the F-CaP coating.

3.2. Microstructure and phase composition analysis

Fig. 3 illustrates XRD patterns of the uncoated AZ60 alloy, and the CaP, HA, and F-CaP coated samples. The AZ60 alloy substrate consisted mainly of an α-Mg solid solution, and the β phase was generally less detectable due to its small quantity. The CaP coating consists mainly of dicalcium phosphate dihydrate (DCPD, $CaHPO_4{\cdot}2H_2O$) and a small quantity of tricalcium phosphate (TCP, $Ca_3(PO_4)_2$). HA became the major phase after the alkali post-treatment, while the diffraction peak position of the F-CaP coating are similar to those of the HA coating, corresponding mainly to the FHA phase, with a similar hexagonal crystal lattice and a slight shift of characteristic peaks to the right.[16] It should be mentioned that TCP and MgF_2 also existed in the F-CaP coating, although their intensity was low compared to that of Mg.

In order to obtain a fuller understanding of the coating composition, the coatings were also analyzed by XPS (Fig. 4). The XPS survey scanning spectrum in Fig. 4a indicates that chemical

composition of all the coatings consisted of O, P, Ca and Mg, except the high concentration of carbon, which is common in XPS analysis due to extraneous hydrocarbons from the environment. The high-resolution spectra of the Ca 2p peak (Fig. 4b) split into two peaks as a result of spin orbit splitting. The binding energy of the Ca 2p3/2 peak of the CaP coating can be fitted to TCP (346.9 eV) and DCPD (347.8 eV) according to Song et al.,[29] while that of the HA coating is 347.8 eV, which is in good agreement with that of HA.[30] Compared to the XPS spectra of the HA coating, the slight right shift of spectra III can be attributed to the existence of a combination of FA (347.9 eV)[31] and TCP (346.9 eV) [29]. The high-resolution spectrum of F 1s of the F-CaP coating as shown in Fig. 4c, with binding energy at 685.1 eV, can be resolved into two components: FHA (684.6 eV)[30] and MgF_2 (685.8 eV).[32] This suggests that F ions have been incorporated into the HA crystalline structure, and that the coating consists mainly of FHA, TCP, and MgF_2. The high-resolution spectra of Mg2p (Fig. 4d) demonstrate the different characteristic peaks of Mg^{2+} on the different coating surfaces. There was no Mg peak detected on the surface of the CaP coating, which indicates the complete coverage of the CaP coating. The Mg2p peaks of the HA and F-CaP coating were too weak to get good fittings. Together with the XRD result and F 1s peak fitting result, it can be confirmed that the higher Mg2p peak for the F-CaP coating can be attributed to the presence of MgF_2 and the lower one for the HA coating is related with the $Mg(OH)_2$.

Typical surface morphologies of the CaP, HA, and F-CaP coatings, as well as EDS results of the F-CaP coating are shown in Fig. 5. It can be observed from Fig. 5a that the Mg alloy substrate is completely covered by the flake-like coating, with randomly distributed flakes of 10-20 μm in length and 1-2 μm in thickness. Fig. 5b-c depict morphologies of the CaP coatings after the alkali

post-treatment and the fluorine post-treatment, respectively. The HA coating (Fig. 5b) exhibits a denser flake-like morphology, which may result from the dissolution and clustering of previous CaP flakes. As for the F-CaP coating, the flower-like microstructure has become denser and smoother than those of the CaP and HA coatings. It should be mentioned that some fine needle-like flakes emerged in the gaps among the coating flakes, where the F content was shown to be extremely high (around 19 at.%) from the EDS spectrum (Fig. 5d) of the red point in Fig. 5c. The EDS spectrum and elemental compositions of the whole coating surface are also listed for comparison in Fig. 5d. Together with the above mentioned XRD and XPS analyses, it can be confirmed that the needle-like flakes are attributable to the formation of MgF_2, which possibly resulted from a reaction between the Mg substrate and the fluoride solution when the solution penetrated the flake-like coating at some weak sites, especially the gaps between coating flakes. It also can be observed that all the coatings are generally not very dense, as some cracks appeared on the coating flakes, which might be attributed to the shrinkage of the coating during SEM imaging.

3.3. Proposed mechanism of the F-CaP coating formation

Since DCPD in the CaP coating is unstable in environments with pH values greater than 6~7,[33] the alkali solution transformed DCPD into in the HA following reaction:

$$10CaHPO_4 \cdot 2H_2O + 12OH^- \rightarrow Ca_{10}(PO_4)_6(OH)_2 + 4PO_4^{3-} + 30H_2O \quad (1)$$

During the fluorine post-treatment, DCPD reacted with the fluoride solution to form FHA:

$$10CaHPO_4 \cdot 2H_2O + xF^- + (12-x)OH^- \rightarrow Ca_{10}(PO_4)_6(OH)_{2-x}F_x + 4PO_4^{3-} + 30H_2O \quad (2)$$

The minor ingredients of the phosphate coating and the Mg substrate reacted with the fluoride solution as well:

$$10Ca_3(PO_4)_2 + 3xF^- + (6-3x)OH^- \rightarrow 3Ca_{10}(PO_4)_6(OH)_{2-x}F_x + 2PO_4^{3-} \quad (3)$$

$$Mg + 2H_2O \rightarrow Mg^{2+} + 2OH^- + H_2\uparrow \quad (4)$$

$$Mg^{2+} + 2NaF \rightarrow MgF_2 + 2Na^+ \quad (5)$$

During the post-treatment, the alkali or fluoride solution penetrated the flaky phosphate coating to dissolve some flakes, and then most caves and micro-pores were filled with the reaction products. Thus, the coating became denser and better adhered onto the substrate, as shown in Fig. 5c-d.

3.4. Electrochemical corrosion behavior of the CaP, HA and F-CaP coated samples

Fig. 6 shows the polarization curves for the uncoated AZ60 alloy, and the CaP, HA, and F-CaP coated samples in the SBF solution at 37 °C. The values of the electrochemical parameters obtained from the polarization curves are summarized in Table 3. It can be clearly seen that, for all the coatings, the E_{corr} and pitting potential (E_{pt}) shifted in the positive direction, the polarization current density decreased, the polarization resistance increased, and obvious passivation occurred in the anodic branch, compared with the uncoated samples. It is noteworthy that the passivation range for the CaP coating reached at 200 mV, which is greater than that of the post-treated coatings. This is possibly related to the porous flake-like microstructure of the conversion coating. In addition, the F-CaP and HA coatings had comparable i_{corr}, but the F-CaP coating had more positive E_{corr} and E_{pt} and much greater R_p (3, 26, 213 times higher than that of the HA, CaP and bare alloy, respectively). In order to further understand the corrosion behavior of the coatings, the EIS was employed. Fig. 7 shows the resulting Nyquist plots for the AZ60 alloy and the coated samples. Three equivalent circuits as shown in Fig. 8 were used to evaluate the impedance spectra depending on the Nyquist plot shape, which describes the type of

electrochemical reactions taking place on the electrode surface.

The Nyquist plot for the AZ60 alloy consisted of one high frequency (HF) capacitive loop, one medium frequency (MF) capacitive loop and one short low frequency (LF) inductive loop. This diagram can be described by the equivalent circuit shown in Fig. 8a. R_s is the solution resistance. A pair of elements R_f and Q_f in parallel describe the HF capacitive loop related to both the charge transfer and a film effect of corrosion products based on $Mg(OH)_2$ that formed during the period for establishing a stable OCP in SBF.[34] Q stands for CPE (constant phase element) and is defined by two values, admittance (Y_0) and power index number (n), given by $Y=Y_0(j\omega)^n$. When n=1, CPE is identical to a capacitor. CPE accounts for the deviation from ideal dielectric behavior and is related to the surface inhomogeneity. Thus it is commonly used in place of capacitance for a better quality fit. The MF loop is attributed to the relaxation of mass transport in the solid phase due to the growth of the corrosion product film.[34] R_{mt} is the mass transfer resistance and C_{dl} represents the electric double layer capacity at the solution/substrate interface at pinholes. R_{ads} and L_{ads} describe the LF inductive loop. The presence of the inductive loop suggests the relaxation of absorbed species, which is generally related to the exposure of the substrate and the subsequent release of Mg^+ ions and $Mg(OH)_2$.[35] The Nyquist plot for the CaP coating contained two capacitive loops without an inductive loop. This diagram was analyzed using the equivalent circuit in Fig. 8b, which reveals the presence of different intersurface areas with different characteristics. The HF capacitive loop is related to the dielectric properties of the coating (characterized by R_c and Q_c), while the LF capacitive loop is related to the solution/substrate interface, and R_{ct} is the charge transfer resistance. The third equivalent circuit shown in Fig. 8c was used to describe the Nyquist plots for the HA and F-CaP coatings. The

plots only contained one capacitance loop, which refers to the simple process at the solution/coaitng interface and implies that the coatings have full coverage and could supply good corrosion protection for the Mg alloy.

The EIS fitting results are listed in Table 4. Compared with the corrosion product film on the bare alloy, all the coatings had lower values of Y_0, suggesting that the coatings were less defective than the corrosion product film. The decreased *n* values for the CaP and HA coatings indicate that the surface became rougher due to the flake-like microstructure (Fig. 5a-b). As for the F-CaP coating, the *n* value increased greatly and even exceeded that of the corrosion product film on the bare alloy. This suggests that the capacitive response from the solution/coaitng interface was enhanced because the coating became smooth with a reduction of the flake-like microstructure. The further reduced Y_0 and increased *n* of the F-CaP coating indicate that this coating became denser and had fewer micro-pores (Fig. 5c). It should be pointed out that the R_c value of the F-CaP coated surface was 9399 $\Omega \bullet cm^2$, which is around 35 times higher than the R_f value of the uncoated surface, and also approximately twice that of the CaP coating. This shows that the fluorine post-treatment made the CaP coating much more effective as a barrier layer in protecting the Mg alloy from corrosion in SBF solution.

3.5. Corrosion behavior and coating evolution during immersion test

When the samples were immersed in SBF, the volume of released H_2 and pH of the SBF were monitored, and the results are shown in Fig. 9. It can be seen that the H_2 volume is lesser for all the coated samples, especially for the F-CaP coating which is about four times less than that of the uncoated alloy over the whole period of 7 days (Fig. 9a). During the initial several hours of

immersion, few hydrogen bubbles appeared on the surfaces of the HA and F-CaP coatings, while large numbers of hydrogen bubbles were observed rising from the surface of the uncoated alloy. The corrosion protection of the coatings is also evidenced by the much smaller variation in pH values of the SBF (Fig. 9b). The pH of the solution with the uncoated alloy increased rapidly from 7.4 to 9.1 on the first day of immersion, then increased slowly with immersion time, and stabilized after 4 days of immersion, possibly due to the coverage of the corrosion products. In contrast, the pH of the solution with the coated samples increased much slower. It reached 7.6 on the first day, and 9 after the immersion test period (15 days) for the F-CaP coating.

In order to further understand the corrosion behavior and evaluate *in vitro* bioactivity of the uncoated AZ60 alloy, and the CaP, HA, and F-CaP coated samples, the SEM images of the these samples after 7 and 15 days of immersion in the SBF solution can be seen in Fig. 10, and their corresponding EDS results are shown in Fig. S2. The corrosion layer together with corrosion pits and cracks can be observed on the bare alloy after 7 days of immersion (Fig. 10a). A small number of outer precipitates, mainly clusters of white floccule, with a Ca/P molar ratio of approximately 1.0 (shown in Fig. S3a), also appeared on the corrosion layer. The corrosion layer was composed of corrosion products based on $Mg(OH)_2$ and could act as the passive layer which were thickening over time, thus the corrosion rate declines after the primary increase (Fig. 9).[36, 37] However, due to the porosity of the $Mg(OH)_2$, the corrosion cannot be completely suppressed. Deep corrosion pits and loosely packed white particles increased with immersion time (Fig. 10b). Due to the severe corrosion after 15 days of immersion, cracks were covered by substantial quantities of corrosion products, and the outer precipitates decreased greatly on the surface, which can also be deduced from the change of the Ca and P contents (Fig. S2a-b).

The SEM morphology of the CaP-coated sample after 7 days of degradation is shown in Fig. 10c. The flake-like coating structure almost disappeared, and was replaced by some clusters of needle-like precipitates on the remaining CaP coating surface. After 15 days of degradation, the coating was cracked with pieces of coating plates left on the surface. However, the outer precipitates showed in situ growth, and needle-like crystals sprang up from the inner corrosion layer and the remaining coating plates. The Ca/P molar ratio for these needle-like precipitates was similar with that for the bare alloy (Fig. S3b). For the HA-coated sample, although the flake-like coating structure was still dissolved out and few precipitates can be observed on the remaining HA, the remaining coating was dense enough to protect the substrate from corroding (Fig. 10e). But after 15 days of immersion, the remaining coating was cracked, leading to the exposure of the underlying substrate to the SBF at the thinly covered edges and the consequent formation of the cracked inner corrosion layer (arrows in Fig. 10f). EDS results in Fig. S2e-f showed that the Ca and P contents of the whole surface were slightly decreased, while those of the Mg and Al increased correspondingly after 15 days of immersion, which revealed the *in vitro* failure of the HA coating possibly initiated at this point. The reduced dissolution rate of the FHA and the dense structure of the F-CaP coating have increased its corrosion resistance, so after 7 days of immersion the substrate was still covered by the flake-like layer, which retained its morphology almost unchanged after 15 days of immersion (Fig. 10h). The cracks appeared on the surface can be possibly due to the dissolution of the MgF_2 in the F-CaP coating. Precipitates on the remaining coating show in situ growth as the small crystals sprang up from the coating flakes (Fig. 11g), and aggregated into clusters of white spheres on the remaining flakes (Fig.

10h). The Ca, P and F contents kept stable (Fig. S2g-h), while the Ca/P molar ratio for these spherical crystals has increased up to 1.1 on average (Fig. S3c).

After immersion in the SBF, the formation of Mg^{2+} and release of H_2 bubbles caused a reduction of H^+ and increased the pH value of the solution, which facilitated the precipitation of insoluble phosphate.[38] This is the main reason why the outer precipitates appeared on the uncoated alloy surface. As for the CaP coating, the coating flakes first dissolved and then the surface was mineralized in the SBF. The dissolution mechanism of Ca and P ions in SBF is dominated mainly by ion exchange[39] and the biomineralization is initiated by the electrostatic interaction of negative surface-charged groups with ions in the fluid.[40, 41] However, there was no obvious biomineralization on the HA coating surface, although this coating was much more corrosion resistant in the SBF. The F-CaP coating was more stable than HA, and the coating flakes still existed after 15 days of immersion. The structural stability, the low solubility and the closely packed organization of the F-CaP coating contribute to its long-term stability and outstanding corrosion resistance. The apatite nucleation and in-situ growth on the coating flakes show that the F-CaP coating is bioactive and could induce surface biomineralization in SBF.

Fig. 11 presents surface appearances of the samples immersed in SBF for 7 and 15 days after corrosion product removal. After 7 days of immersion, some detached corrosion products were observed at the bottom of the beaker containing the uncoated alloy. As shown in Fig. 11a, the surface showed numerous traces of filiform corrosion, which also emerged on the CaP-coated surface. The HA-coated sample surface showed much slighter pitting corrosion in specific locations, particularly on the edges, where the coating coverage was relatively weaker. It is noted

that the CaP-coated sample was more susceptible to corrosion than the HA- and F-CaP-coated samples, which can be explained by the porous nature of the CaP coating. It has been reported that an increase in surface roughness led to an increase in general corrosion rate.[42] No obvious corrosion but some white spots were observed on the F-CaP coating surface (Fig. 11d), and the coating surface was not as uniform as before immersion. This indicates that some coating structures were dissolved in SBF, but the aggressive solution did not penetrate the coating due to the dense microstructure of the coating and the low solubility of FHA. The corrosion that occurred in the first 7 days resulted in the formation of a rather rough surface, which accelerated further corrosion. So all the surfaces after 15 days showed evidence of more serious corrosion attack. In particular, a great number of corrosion cavities and filiform corrosion traces connected together, and were distributed across the whole surface of the uncoated alloy (Fig. 11e). Although some short corrosion traces originating from the edges appeared, most of the F-CaP-coated surface was not attacked (Fig. 11h).

So it can be concluded that the presence of the CaP and HA coatings inhibits the corrosion at the initial stage (around 7 days for the HA coating), while the F-CaP coating can protect the alloy for the first 15 days. The ranking of the corrosion protection performance is as follows: F-CaP coating > HA coating > CaP coating > AZ60 alloy. Therefore, due to the clearly shown improvement on degradation behavior of the F-CaP-coated samples, the fluorine post-treatment increases the potential usefulness of the CaP coating on Mg alloys for orthopedic implant applications. Even though there is no toxic element detected in the coating, some biological assessments may be necessary to confirm its cytocompatibility.

4. Conclusions

Through a simple fluorine post-treatment, the calcium phosphate (CaP) conversion coating on AZ60 magnesium alloy surface was transformed into F-CaP composite coating, consisting mainly of fluoridated hydroxyapatite (FHA), tricalcium phosphate (TCP) and magnesium fluoride (MgF_2). The pH of the fluorine post-treatment solution and treatment time greatly affect the electrochemical corrosion resistance of the post-treated coating, and the optimum fluorine post-treatment parameters were confirmed at pH 12 and 2 h treatment time. The F-CaP coating dramatically reduces degradation rate of the alloy based on the electrochemical and immersion test results in simulated body fluid. In addition, it also shows improved corrosion protectiveness and better surface bioactivity than the CaP and HA coatings. The fluorine post-treatment not only broadens the method for the preparation of FHA coatings, but also offers a novel and practical approach to improving the biodegradation behavior of CaP coatings on biodegradable magnesium implants for orthopedic applications.

Acknowledgements

The authors would like to thank Prof. Hendra Hermawan (Laval University, Canada) for assisstance in the manuscript review and revisions. This work was supported by the National Nature Science Foundation of China (Grant No. 31070841).

References

1. M. P. Staiger, A. M. Pietak, J. Huadmai and G. Dias, *Biomaterials*, 2006, **27**, 1728-1734.
2. Y. Xin, T. Hu and P. K. Chu, *Acta Biomater.*, 2011, **7**, 1452-1459.
3. Y. F. Zheng, X. N. Gu and F. Witte, *Mat. Sci. Eng. R*, 2014, **77**, 1-34.
4. N. L. Saris, E. Mervaala, H. Karppanen, J. A. Khawaja and A. Lewenstam, *Clin. Chim. Acta*, 2000, **294**, 1-26.
5. F. Witte, N. Hort, C. Vogt, S. Cohen, K. U. Kainer, R. Willumeit and F. Feyerabend, *Curr. Opin. Solid. St. M.*, 2008, **12**, 63-72.
6. S. V. Dorozhkin, *Acta Biomater.*, 2014, **10**, 2919-2934.
7. S. Shadanbaz and G. J. Dias, *Acta Biomater.*, 2012, **8**, 20-30.
8. R. A. Surmenev, M. A. Surmeneva and A. A. Ivanova, *Acta Biomater.*, 2014, **10**, 557-579.
9. S. R. Paital and N. B. Dahotre, *Mat. Sci. Eng. R*, 2009, **66**, 1-70.
10. K. J. L. Burg, S. Porter and J. F. Kellam, *Biomaterials*, 2000, **21**, 2347-2359.
11. Y. Chen and X. Miao, *Ceram. Int.*, 2004, **30**, 1961-1965.
12. E. Lee, S. Lee, H. Kim, Y. Kong and H. Kim, *Biomaterials*, 2005, **26**, 3843-3851.
13. K. A. Bhadang and K. A. Gross, *Biomaterials*, 2004, **25**, 4935-4945.
14. K. Cheng, W. Weng, H. Wang and S. Zhang, *Biomaterials*, 2005, **26**, 6288-6295.
15. B. D. Hahn, Y. L. Cho, D. S. Park, J. J. Choi, J. Ryu, J. W. Kim, C. W. Ahn, C. Park, H. E. Kim and S. G. Kim, *J. Biomater. Appl.*, 2012, **27**, 587-594.
16. Y. Song, S. Zhang, J. Li, C. Zhao and X. Zhang, *Acta Biomater.*, 2010, **6**, 1736-1742.
17. J. Li, Y. Song, S. Zhang, C. Zhao, F. Zhang, X. Zhang, L. Cao, Q. Fan and T. Tang, *Biomaterials*, 2010, **31**, 5782-5788.
18. H. R. Bakhsheshi-Rad, E. Hamzah, M. Daroonparvar, R. Ebrahimi-Kahrizsangi and M. Medraj, *Ceram. Int.*, 2014, **40**, 7971-7982.
19. E. C. Meng, S. K. Guan, H. X. Wang, L. G. Wang, S. J. Zhu, J. H. Hu, C. X. Ren, J. H. Gao and Y. S. Feng, *Appl. Surf. Sci.*, 2011, **257**, 4811-4816.
20. Y. W. Song, D. Y. Shan and E. H. Han, *Mater. Lett.*, 2008, **62**, 3276-3279.
21. M. Kumar, H. Dasarathy and C. Riley, *J. Biomed. Mater. Res.*, 1999, **45**, 302-310.
22. M. Metikoš-Huković, R. Babić, Z. Grubač, M. Petravić and R. Peter, *J. Electrochem. Soc.*, 2013, **160**, H674-

H680.

23. X. B. Chen, N. Birbilis and T. B. Abbott, *Corros. Sci.*, 2011, **53**, 2263-2268.
24. R. Narayanan, S. K. Seshadri, T. Y. Kwon and K. H. Kim, *J. Biomed. Mater. Res. B: Applied Biomaterials*, 2008, **85B**, 279-299.
25. J. Redepenning, T. Schlessinger, S. Burnham, L. Lippiello and J. Miyano, *J. Biomed. Mater. Res.*, 1996, **30**, 287-294.
26. Y. Su, G. Li and J. Lian, *Int. J. Electrochem. Sci.*, 2012, **7**, 11497-11511.
27. G. Song, *Corros. Sci.*, 2007, **49**, 1696-1701.
28. Y. Su, L. Niu, Y. Lu, J. Lian and G. Li, *J. ELECTROCHEM SOC*, 2013, **160**, C536-C541.
29. Y. Song, D. Shan, R. Chen, F. Zhang and E. H. Han, *Corros. Sci.*, 2009, **51**, 62-69.
30. W. J. Landis and J. R. Martin, *J. Vac. Sci. Technol. A*, 1984, **2**, 1108-1111.
31. Y. Barbaux, M. Dekiouk, D. Le Maguer, L. Gengembre, D. Huchette and J. Grimblot, *Appl. Catal. A-Gen.*, 1992, **90**, 51-60.
32. C. D. Wagner, *J. Electron. Spectrosc.*, 1980, **18**, 345-349.
33. B. S. Strates, W. F. Neuman and G. J. Levinskas, *J. Phys. Chem.*, 1957, **61**, 279-282.
34. M. Anik and G. Celikten, *Corros. Sci.*, 2007, **49**, 1878-1894.
35. Y. C. Yang, C. Y. Tsai, Y. H. Huang and C. S. Lin, *J. Electrochem. Soc.*, 2012, **159**, C226-C232.
36. X. N. Gu, W. Zheng, Y. Cheng and Y. F. Zheng, *Acta Biomater.*, 2009, **5**, 2790-2799.
37. M. Razavi, M. Fathi, O. Savabi, S. Mohammad Razavi, B. Hashemi Beni, D. Vashaee and L. Tayebi, *Ceram. Int.*, 2014, **40**, 3865-3872.
38. L. Kouisni, M. Azzi, M. Zertoubi, F. Dalard and S. Maximovitch, *Surf. Coat. Tech.*, 2004, **185**, 58-67.
39. Q. Zhang, J. Chen, J. Feng, Y. Cao, C. Deng and X. Zhang, *Biomaterials*, 2003, **24**, 4741-4748.
40. K. Y. Lee, M. Park, H. M. Kim, Y. J. Lim, H. J. Chun, H. Kim and S. H. Moon, *Biomed. Mater.*, 2006, **1**, R31-R37.
41. M. Tanahashi and T. Matsuda, *J. Biomed. Mater. Res.*, 1997, **34**, 305-315.
42. A. Shahryari, W. Kamal and S. Omanovic, *Mater. Lett.*, 2008, **62**, 3906-3909.

Figure Captions:

Fig. 1 Polarization curves of fluorine post-treated coatings obtained at (a) different pH values and (b) different treatment times.

Fig. 2 Surface morphologies and corresponding EDS results of fluorine post-treated coatings obtained at different pH values of (a) 10, (b) 12, (c) 13 for 2 h; and (d) for 6h at pH=12.

Fig. 3 (a) XRD patterns of (I) uncoated, (II) CaP, (III) HA and (IV) F-CaP coated Mg alloy.

Fig. 4 XPS spectra of (I) CaP, (II) HA and(III) F-CaP coated Mg alloy: (a) survey scanning spectrum; (b) high-resolution spectrum of Ca 2p; (c) high-resolution spectrum of F 1s; (d) high-resolution spectrum of Mg 2p.

Fig. 5 Surface morphologies of (a) CaP, (b) HA and (c) F-CaP coatings, and (d) the EDS results of the F-CaP coating.

Fig. 6 Polarization curves of the uncoated AZ60 alloy, and the CaP, HA, and F-CaP coated samples in SBF.

Fig. 7 EIS Nyquist plots of the AZ60 alloy, the CaP, HA and F-CaP coatings in SBF.

Fig. 8 Equivalent circuits for Nyquist plots of (a) uncoated AZ60 alloy, (b) CaP, (c) HA and F-CaP coatings.

Fig. 9 (a) Volume of released H_2 and (b) pH of the SBF as a function of immersion time in immersion test.

Fig. 10 Surface morphologies of (a, b) the uncoated AZ60 alloy, and (c, d) the CaP, (e, f) HA and (g, h) F-CaP coated samples immersed in SBF for (a, c, e, g) 7 days and (b, d, f, h) 15 days.

Fig. 11 Surface appearances of the uncoated and coated samples immersed in SBF for (a-d) 7 days and (e-h) 15 days after removing corrosion products.

Table 1 Chemical composition of the AZ60 magnesium alloy (in wt.%)

Al	Zn	Mn	Si	Cu	Ni	Fe	Mg
5.8~7.2	<1.0	0.15~0.5	≤0.10	≤0.05	≤0.005	≤0.005	Balance

Table 2 Electrochemical parameters obtained from the polarization curves in Fig. 1.

pH value (2h)	E_{corr} *(mV/SCE)*	i_{corr} *($\mu A/cm^2$)*	R_p *($\Omega \cdot cm^2$)*	E_{pt} *(mV/SCE)*
10	-1596	4.0	3756	--
11	-1274	1.0	27087	-1169
12	-1037	0.6	111020	-885
13	-1229	5.9	11948	-939
treatment time (*h*) (pH=12)	E_{corr} *(mV/SCE)*	i_{corr} *($\mu A/cm^2$)*	R_p *($\Omega \cdot cm^2$)*	E_{pt} *(mV/SCE)*
0.5	-1422	1.6	13990	-1243
1	-1249	1.3	15574	-1163
2	-1037	0.6	111020	-885
6	-1351	0.4	49941	-1302

Table 3 Electrochemical parameters obtained from the polarization curves in Fig. 6.

	E_{corr} (mV/SCE)	I_{corr} (μA/cm^2)	R_p (Ω·cm^2)	E_{pt} (mV/SCE)
AZ60 alloy	-1421	33	519	-1440
CaP coating	-1395	13	4175	-1195
HA coating	-1312	0.8	38126	-1142
F-CaP coating	-1037	0.6	111020	-885

Table 4 Fitting results of EIS plots of the AZ60 alloy, DCPD and the HA coatings in the SBF solution.

	R_s (Ω•c m^2)	Y_0 ($\times 10^{-6}$ $\Omega^{-1}cm^{-2}s^n$)	n	$R_c(R_f)$ (Ω•cm^2)	C_{dl} ($\mu F/cm^2$)	R_{ct} (R_{mt}) (Ω•cm^2)	L_{ads} (H/cm^2)	R_{ads} (Ω•cm^2)
AZ60 alloy	13.1	10.5	0.91	267.8	186.4	142	54	183
CaP coating	11.6	2.6	0.83	6507	24.2	1675		
HA coating	16.7	4.8	0.81	8362				
F-CaP coating	16.7	2.3	0.93	9399				

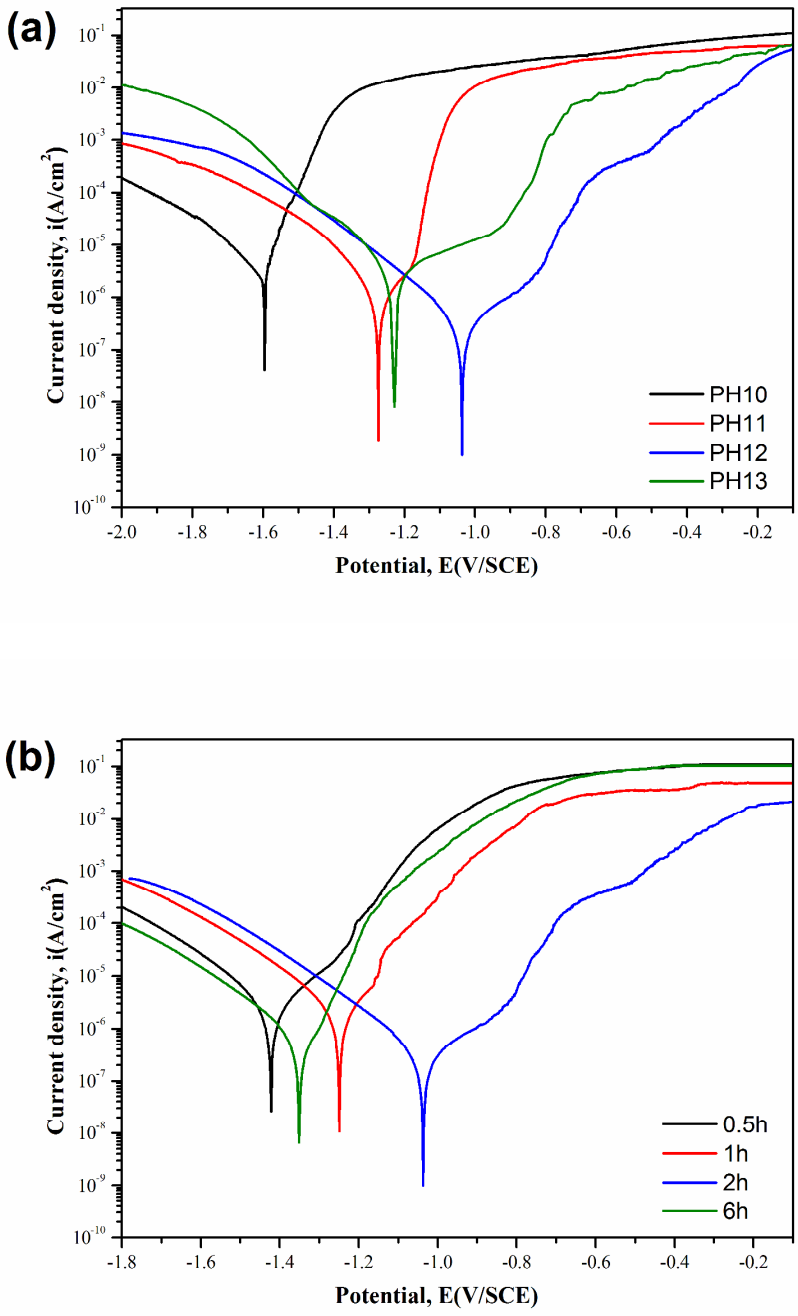

Fig. 1 Polarization curves of fluorine post-treated coatings obtained at (a) different pH values and (b) different treatment times.

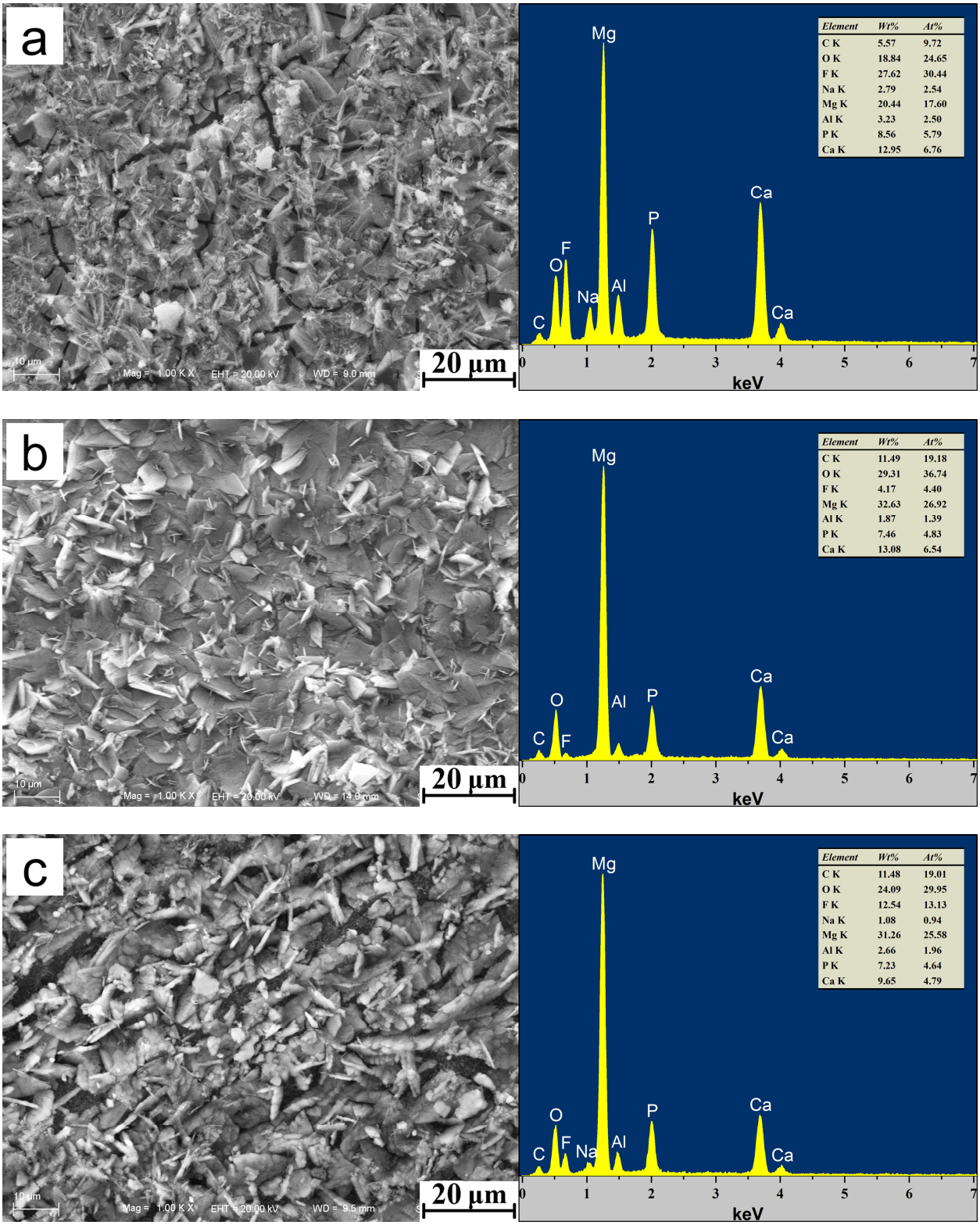
a
Mg
F
O
Na
Al
P
Ca
C
Ca
Element Wt% At%
C K 5.57 9.72
O K 18.84 24.65
F K 27.62 30.44
Na K 2.79 2.54
Mg K 20.44 17.60
Al K 3.23 2.50
P K 8.56 5.79
Ca K 12.95 6.76
10 µm
Mag = 1.00 K X EHT = 20.00 kV WD = 9.0 mm
20 µm
0 1 2 3 4 5 6 7
keV
b
Mg
O
Al
P
Ca
C
F
Ca
Element Wt% At%
C K 11.49 19.18
O K 29.31 36.74
F K 4.17 4.40
Mg K 32.63 26.92
Al K 1.87 1.39
P K 7.46 4.83
Ca K 13.08 6.54
10 µm
Mag = 1.00 K X EHT = 20.00 kV WD = 14.0 mm
20 µm
0 1 2 3 4 5 6 7
keV
c
Mg
O
F
Na
Al
P
Ca
C
Ca
Element Wt% At%
C K 11.48 19.01
O K 24.09 29.95
F K 12.54 13.13
Na K 1.08 0.94
Mg K 31.26 25.58
Al K 2.66 1.96
P K 7.23 4.64
Ca K 9.65 4.79
10 µm
Mag = 1.00 K X EHT = 20.00 kV WD = 9.5 mm
20 µm
0 1 2 3 4 5 6 7
keV

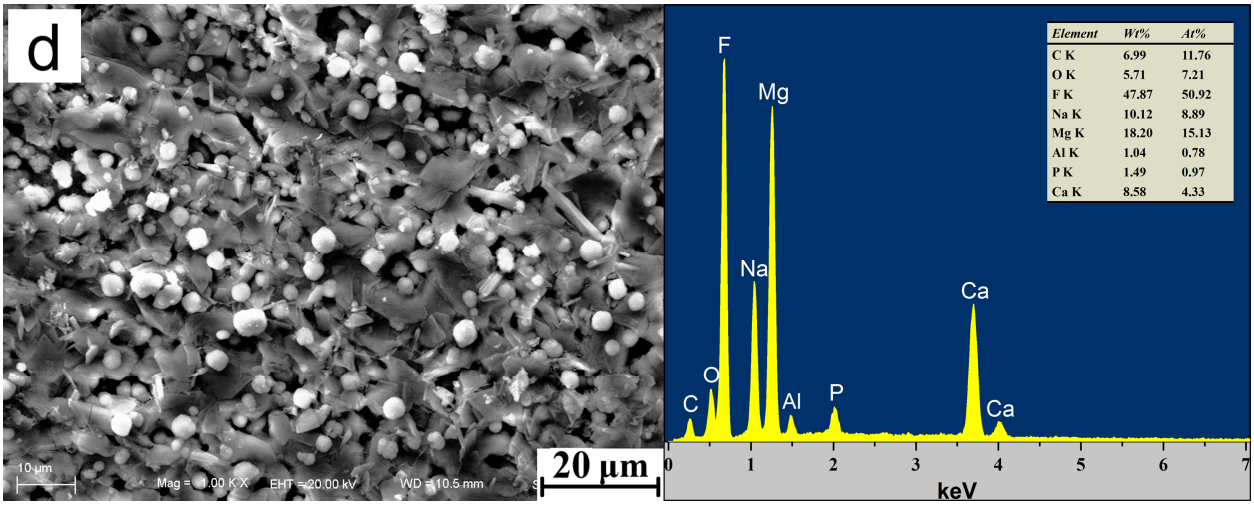

Fig. 2 Surface morphologies and corresponding EDS results of fluorine post-treated coatings obtained at different pH values of (a) 10, (b) 12, (c) 13 for 2 h; and (d) for 6h at pH=12.

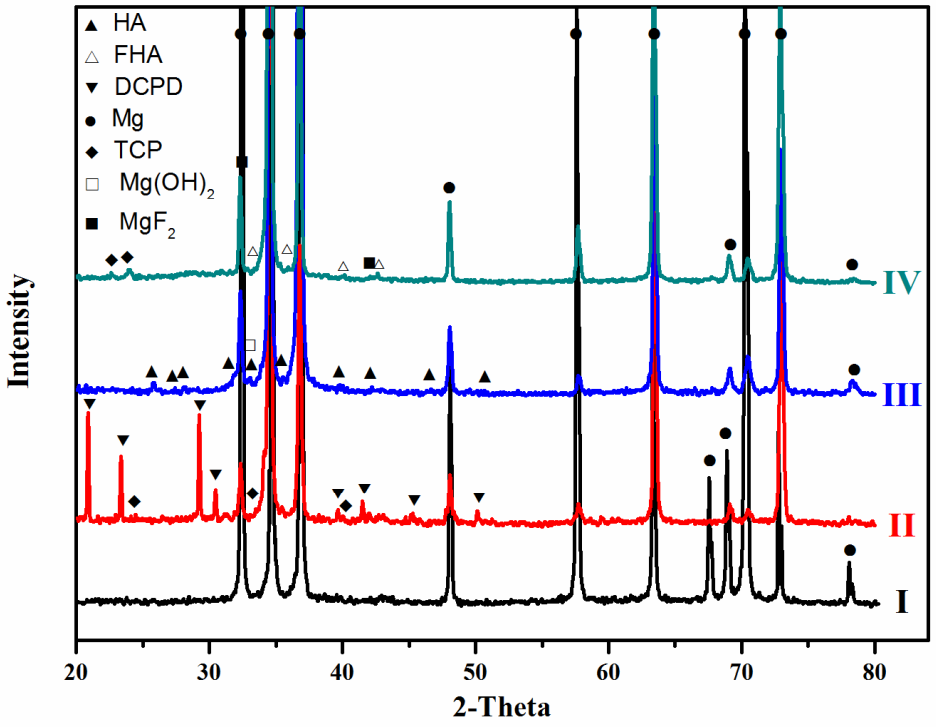

Fig. 3 (a) XRD patterns of (I) uncoated, (II) CaP, (III) HA and (IV) F-CaP coated Mg alloy.

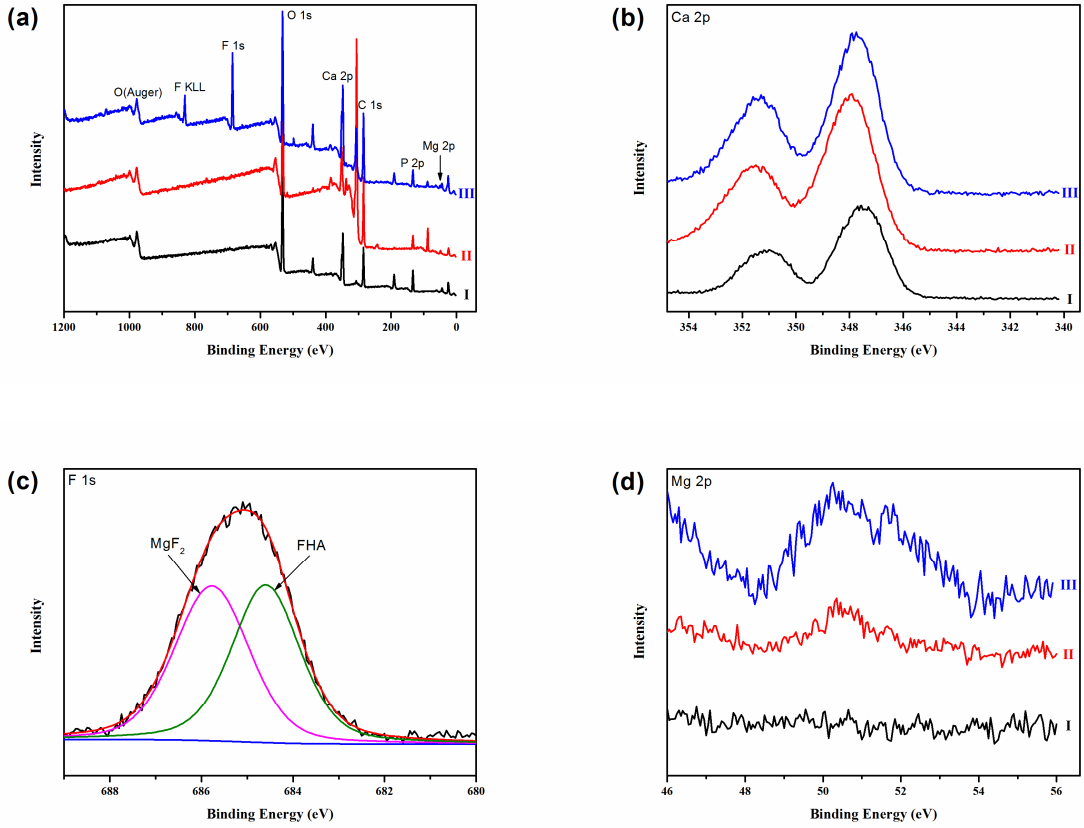

Fig. 4 XPS spectra of (I) CaP, (II) HA and (III) F-CaP coated Mg alloy: (a) survey scanning spectrum; (b) high-resolution spectrum of Ca 2p; (c) high-resolution spectrum of F 1s; (d) high-resolution spectrum of Mg 2p.

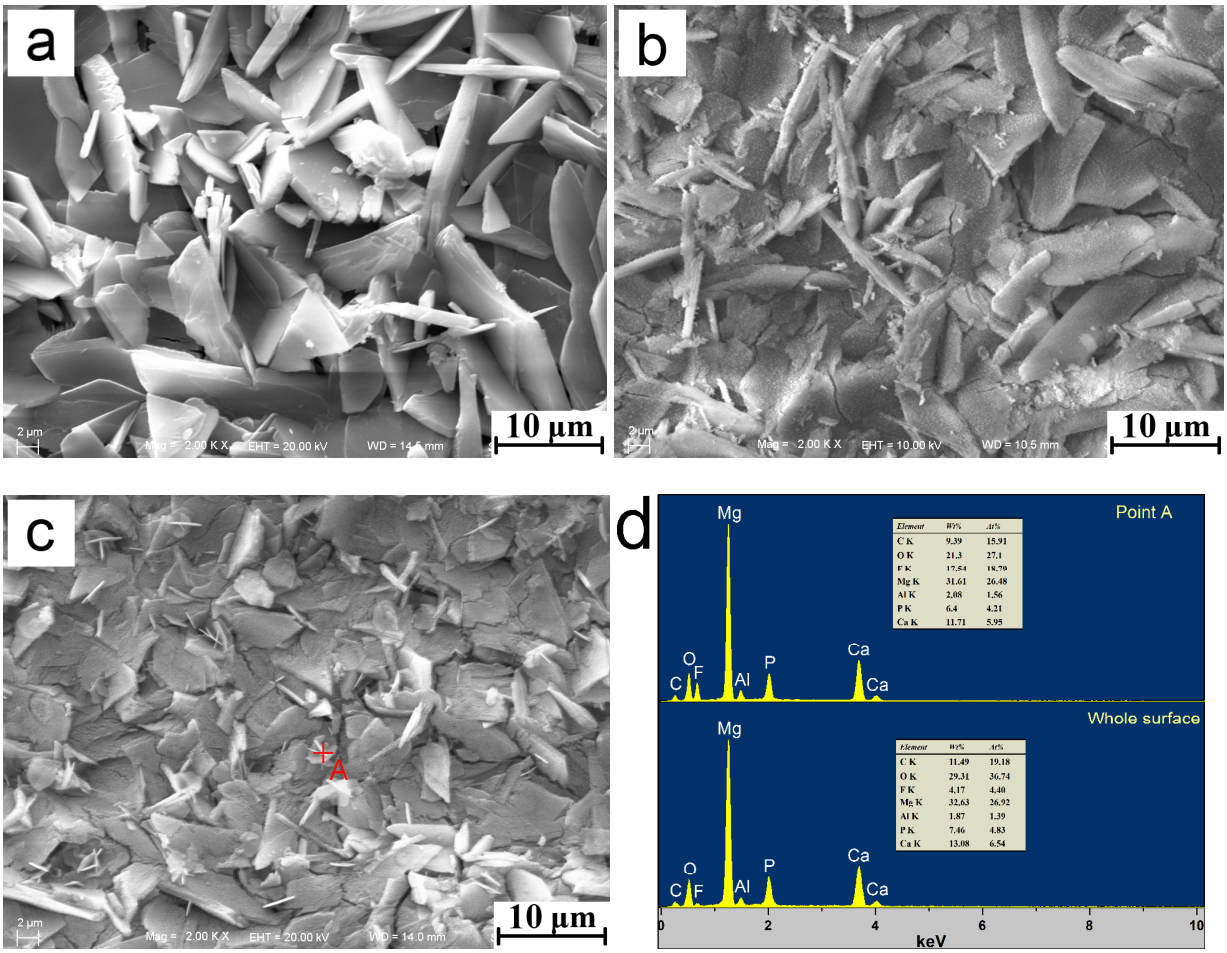

Fig. 5 Surface morphologies of (a) CaP, (b) HA and (c) F-CaP coatings, and (d) the EDS results of the F-CaP coating.

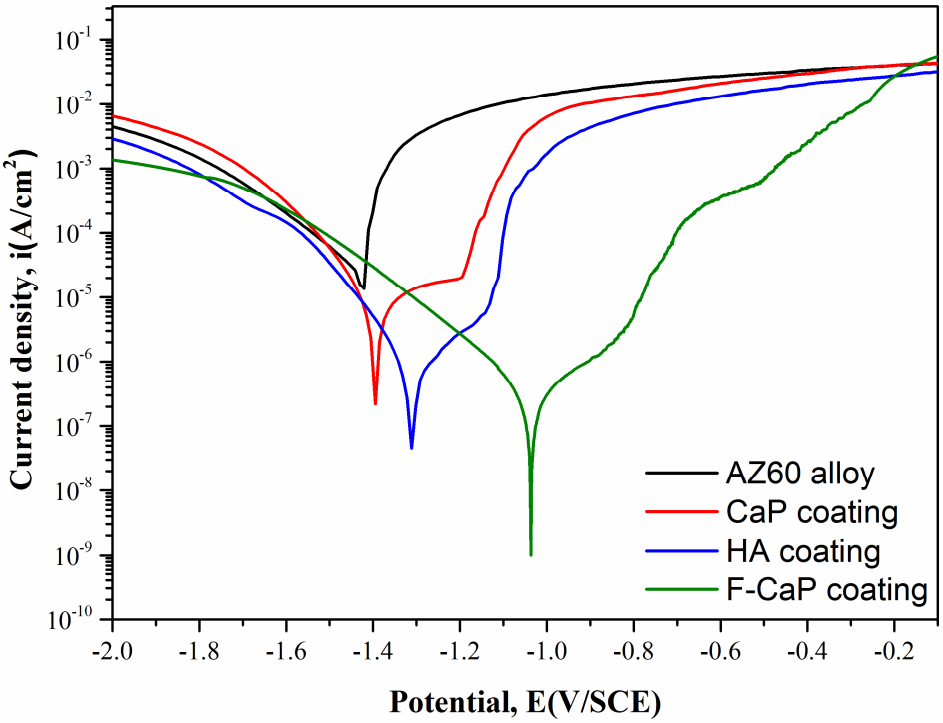

Fig. 6 Polarization curves of the uncoated AZ60 alloy, and the CaP, HA, and F-CaP coated samples in SBF.

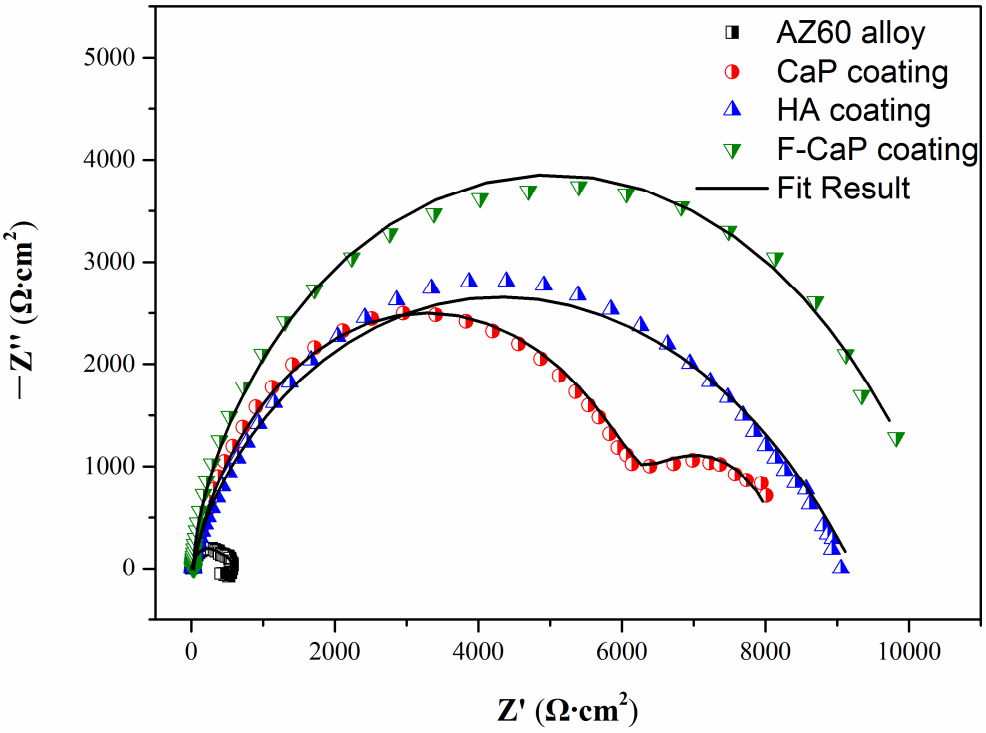

Fig. 7 EIS Nyquist plots of the AZ60 alloy, the CaP, HA and F-CaP coatings in SBF.

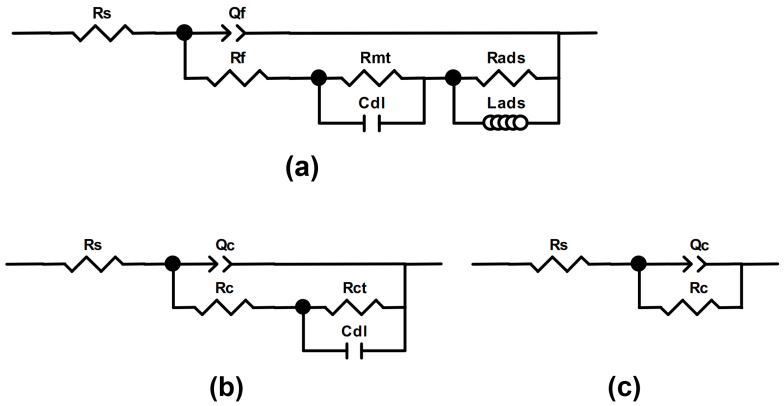

Fig. 8 Equivalent circuits for Nyquist plots of (a) uncoated AZ60 alloy, (b) CaP, (c) HA and F-CaP coatings.

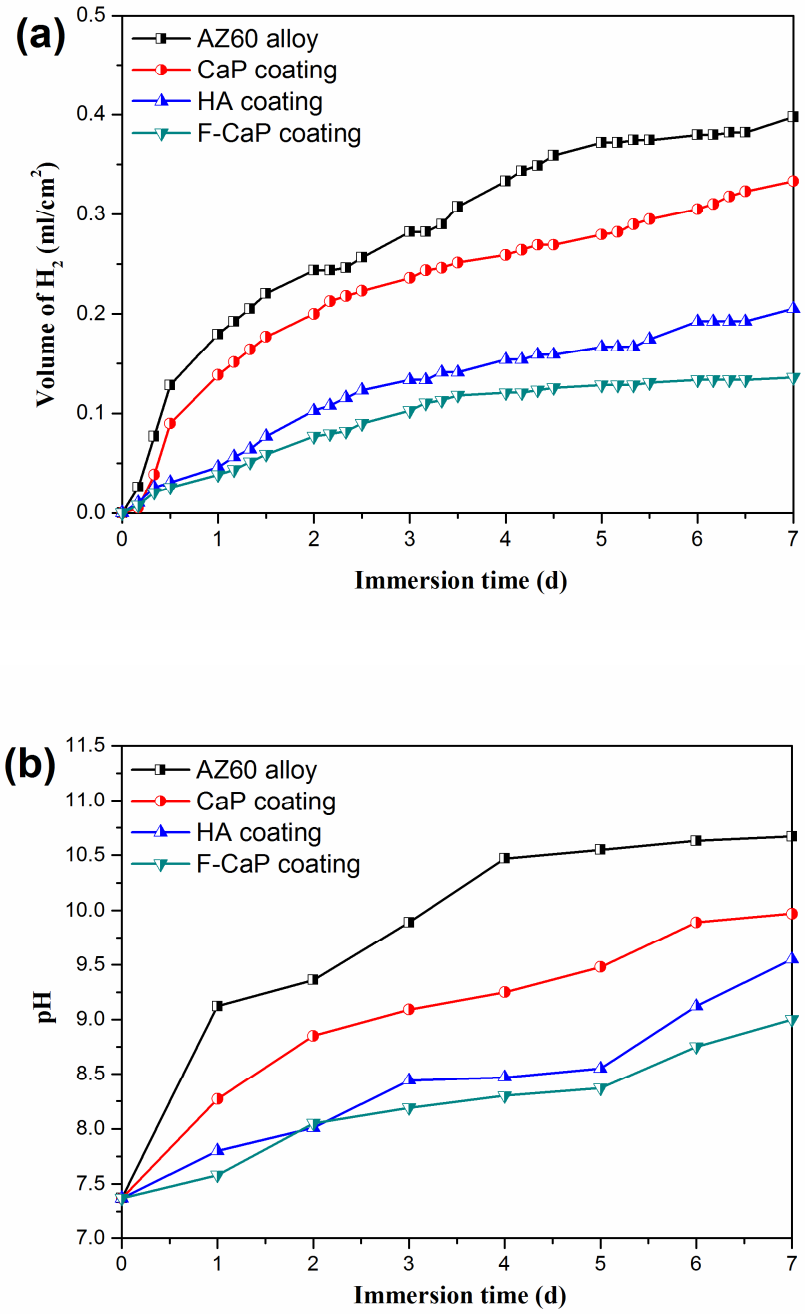

Fig. 9 (a) Volume of released H_2 and (b) pH of the SBF as a function of immersion time in immersion test.

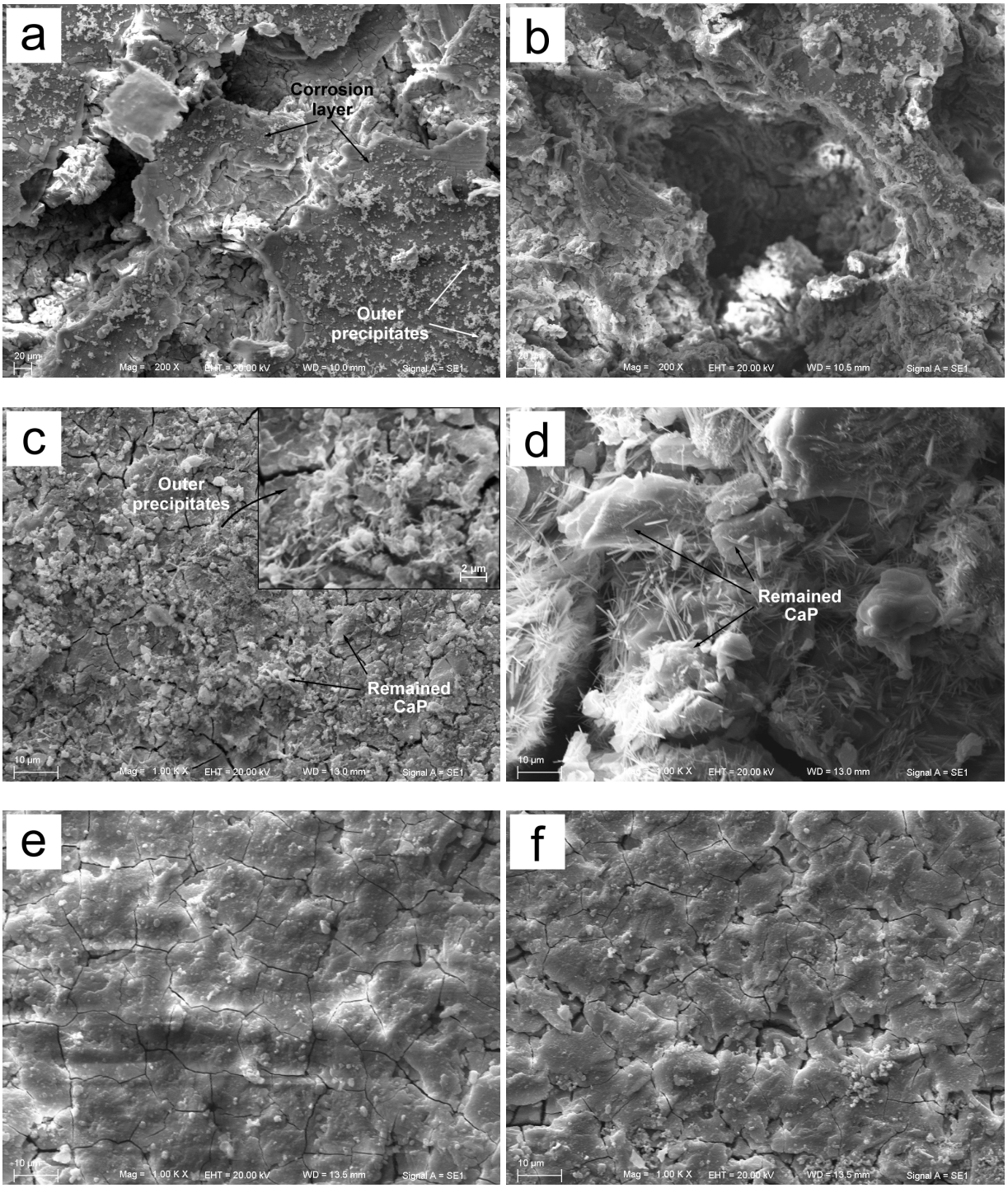
a
Corrosion layer
Outer precipitates
20 µm
Mag = 200 X EHT = 20.00 kV WD = 10.0 mm Signal A = SE1
b
Mag = 200 X EHT = 20.00 kV WD = 10.5 mm Signal A = SE1
c
Outer precipitates
2 µm
Remained CaP
10 µm
Mag = 1.00 K X EHT = 20.00 kV WD = 13.0 mm Signal A = SE1
d
Remained CaP
10 µm
Mag = 1.00 K X EHT = 20.00 kV WD = 13.0 mm Signal A = SE1
e
10 µm
Mag = 1.00 K X EHT = 20.00 kV WD = 13.5 mm Signal A = SE1
f
10 µm
Mag = 1.00 K X EHT = 20.00 kV WD = 13.5 mm Signal A = SE1

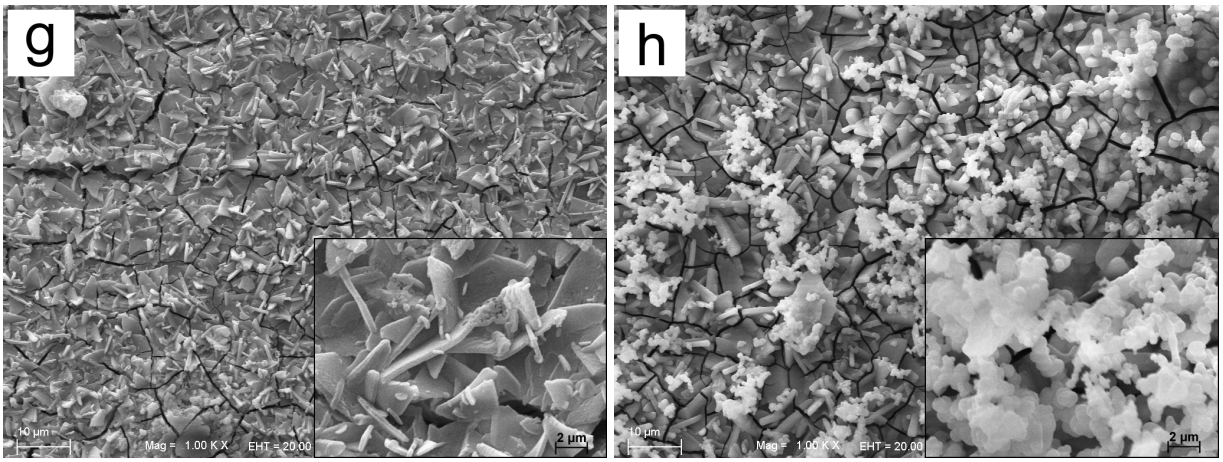

Fig. 10 Surface morphologies of (a, b) the uncoated AZ60 alloy, and (c, d) the CaP, (e, f) HA and (g, h) F-CaP coated samples immersed in SBF for (a, c, e, g) 7 days and (b, d, f, h) 15 days.

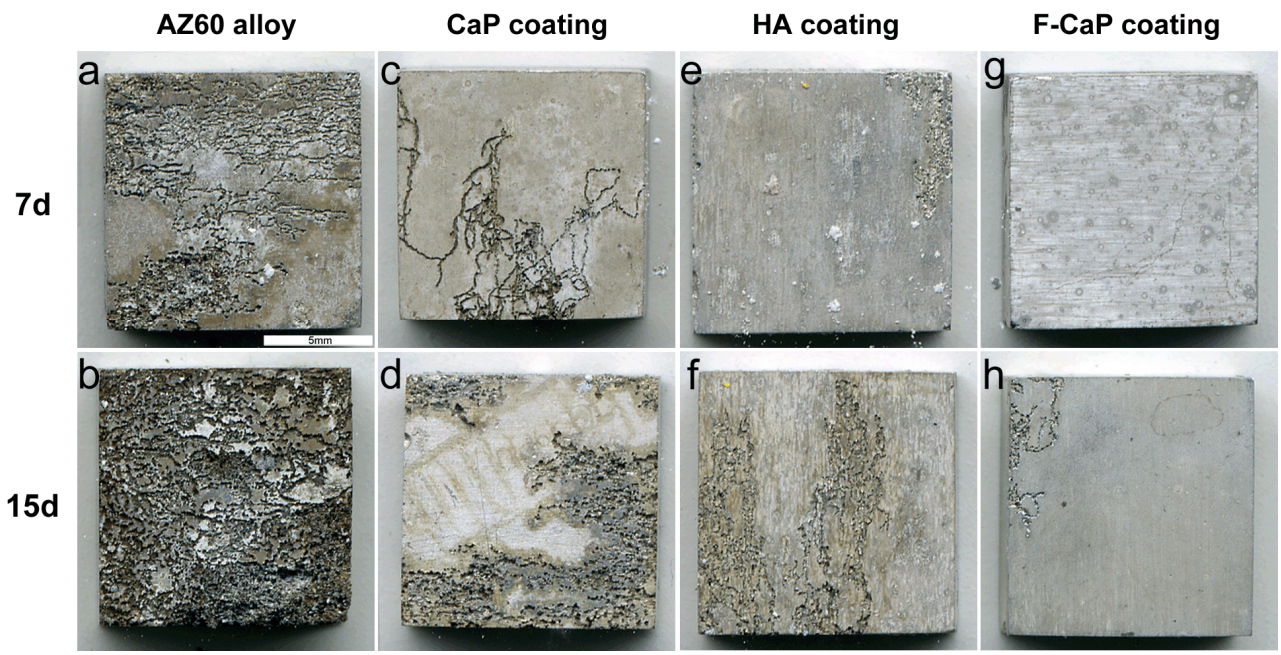

Fig. 11 Appearance photographs of the uncoated and coated samples immersed in SBF for (a-d) 7 days and (e-h) 15 days after removing corrosion products.